Proceedings of ASME-JSME-KSME Joint Fluids Engineering Conference 2011
AJK2011-FED
July 24-29, 2011, Hamamatsu, Shizuoka, JAPAN

AJK2011-20002

FAST AND ACCURATE SIMULATION OF STRONGLY COUPLED FLUID-STRUCTURE INTERACTION USING A DIRECT FORCING IMMERSED BOUNDARY METHOD

Jianming Yang *
IIHR – Hydroscience and Engineering
University of Iowa
Iowa City, IA 52242
Email: jianming-yang@uiowa.edu

Frederick Stern
IIHR – Hydroscience and Engineering
University of Iowa
Iowa City, IA 52242
Email: frederick-stern@uiowa.edu

ABSTRACT

In this paper, a direct forcing immersed boundary method is presented for the simple and efficient simulation of strongly coupled fluid-structure interaction. The previous formulation by Yang and Balaras (An embedded-boundary formulation for large-eddy simulation of turbulent flows interacting with moving boundaries, J. Comput. Phys. 215 (2006) 12-40) is greatly simplified without sacrificing the overall accuracy. The fluid-structure coupling scheme of Yang et al. (A strongly-coupled, embedded-boundary method for fluid-structure interactions of elastically mounted rigid bodies, J. Fluids Struct. 24 (2008) 167-182) is also significantly expedited without altering the strong coupling property. Several cases are examined and compared with the results from the previous formulations to demonstrate the accuracy, simplicity and efficiency of the new method.

INTRODUCTION

The direct forcing immersed boundary methods using discrete momentum forcing terms have been well received among the developers and practitioners of non-boundary conforming methods in the computational fluid dynamics (CFD) field, mainly because of the simplicity of the concept and the ease of the implementation of these methods. Initially, the developments were focused on stationary immersed boundaries ([1]; [2]; [3]; [4]); and very few were applied to problems with moving boundaries, due to that the implications of boundary movement on a fixed grid in a time-splitting scheme, such as the fractional-step method, were not systematically addressed. Then Yang and Balaras [5] demonstrated that, non-physical historical information may enter the flow field in a time step when some grid points with reconstructed solutions at the previous time step become normal fluid points if no treatment is applied to recover the correct historical information at these points. They proposed a field extension strategy that, at the end of each time step, the flow field is extended into the grid points with non-physical values near the immersed boundary through extrapolations. A variety of examples ranging from laminar to turbulent flows were given to show the accuracy and effectiveness of this approach. They further extended it in [6] to fluid-structure interaction (FSI) problems with multiple rigid bodies using a strong coupling scheme in which the structural dynamics was solved via the Hamming's fourth-order predictor-corrector algorithm. In their strong coupling scheme, the fluid and the structure are treated as elements of a single dynamical system, and both sets of governing equations are integrated simultaneously and interactively in the time domain. It is a very efficient iterative scheme as the number of iterations does not change much with increasing the number of degrees of freedom of the structural part and the convergence of the whole coupled system usually is reached within less than ten iterations. In addition, it is not limited to FSI problems with solid bodies, for example, in [7], it was used to study the aerodynamic performance of a flexible hovering wing.

In general, the approaches discussed above for FSI problems (prescribed motion in [5] and predicted motion in [6], re-

*Address all correspondence to this author.

spectively) are quite straightforward and efficient. One issue with the field extension strategy is that the definition of pressure points requiring the extension operation is not as simple as that for velocity points. Instead of a simple geometric relationship, for instance, the closest grid points to the immersed boundary along grid lines (for velocity components, closest grid points in the fluid phase and solid phase are defined as forcing points and pseudo forcing points, respectively, in [5]), the status of all surrounding velocity points (four/six in two-/three-dimensional cases) has to be used to define a pressure point. And such a point may be in either the fluid or the solid phase, depending on the configuration of the immersed boundary and the grid layout. This is not particularly convenient in terms of algorithm design and implementation. Furthermore, for grid points in the solid requiring field extension operation, sometimes ambiguities may exist near sharp corners or under-resolved regions with regard to the normal directions to the immersed boundary. To remove these ambiguities, significant amount of coding work is needed and the clarity and efficiency of the algorithm may be affected. On the other hand, as each fluid-structure iteration in the strong coupling scheme given in [6] involves the complete solutions of both sets of equations, this scheme can be still quite expensive for complicated cases, such as two-phase flows and adaptive mesh refinement, where fast Poisson solvers are not available or straightforwardly applicable. Another strong coupling scheme with immersed boundary method in [8] avoided the iterations by using a non-inertial reference frame fixed to the body. This scheme can be very efficient for some applications, although it is limited to a single solid body and the use of a non-inertial reference frame makes the boundary conditions, especially, inflow and outflow, difficult to handle.

The objective of this work is to address the issues mentioned above. We shall reformulate the pressure field extension and eliminate the cumbersome process of identification and extrapolation of pressure points requiring the extension operation. With the new formulation we are able to accelerate the whole computation several times or even one order of magnitude comparing to the original method in [6].

The rest of this paper is organized as follows: In the next section the mathematical model for FSI problems is introduced. Then in the numerical methods section, following a summary of the original approaches in [5] and [6], our current approach is discussed in detail. In the results section, the accuracy of the reformulated field extension strategy is evaluated using a case with prescribed motion, then two FSI problems are used to demonstrate the efficiency and applicability of our new algorithm.

MATHEMATICAL MODEL

The computational domain for a FSI problem consists of the fluid and structural domains. In this work, a primitive variable method is used for the fluid domain, i.e., the velocity **u** and pressure p are the unknown variables of fluid flow field. For the structural part, the displacement **d** is chosen as the unknown field variable and, correspondingly, the structural boundary can be easily defined. In an immersed boundary approach, usually a Cartesian grid is used to cover the whole domain, which means the structural boundary or the fluid-structure interface, Γ, has to be defined (and tracked for moving boundary problems) on the fixed Cartesian grid as well. On the other hand, since the focus of this work is on the incompressible flow interacting with moving bodies, the introduction of body-fixed non-inertial reference frames facilitate the solution of rigid body dynamics naturally. Therefore, the coordinate systems used in the present study is discussed first.

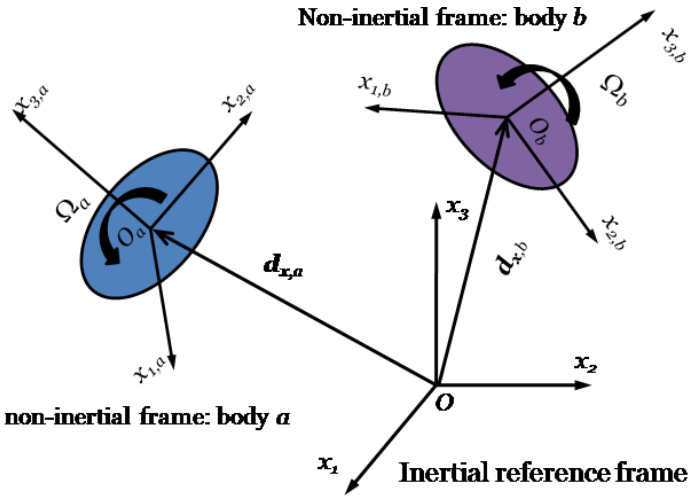

FIGURE 1. RELATIONSHIP BETWEEN THE INERTIAL AND NON-INERTIAL REFERENCE FRAMES.

Coordinate Systems

As shown in Fig. 1, two types of coordinate systems are usually used in FSI problems: an inertial reference frame fixed to or moving at a constant velocity with respect to the earth, and numerous non-inertial reference frames with each attached to a moving body under consideration. All fluid variables are conveniently defined in the inertial reference frame, whereas for a moving body, the motion can be described by the linear and angular displacement with respect to the inertial reference frame, and the linear and angular velocity with respect to the its own body-fixed non-inertial reference frame.

For example, the translational displacement of body a is given by

$$\mathbf{d}_a = (x_{O_a}, y_{O_a}, z_{O_a})^T, \tag{1}$$

in the inertial reference frame. It is the position vector of the

origin, usually chosen to coincide with the center of mass, for the non-inertial reference frame attached to body a. And

$$\Theta_a = (\phi_a, \theta_a, \psi_a)^T \tag{2}$$

gives the three Euler angles for defining the orientation of body a. For simplicity, subscript will be omitted hereafter. On the other hand, the linear and angular velocities of the body are defined as

$$\mathbf{v} = (v_x, v_y, v_z)^T, \tag{3}$$
$$\Omega = (\Omega_x, \Omega_y, \Omega_z)^T \tag{4}$$

with respect to the non-inertial reference frame, respectively.

Therefore, a position vector in the non-inertial reference frame can be transformed back into a vector in the inertial reference frame through a linear transformation given by the linear translation $\mathbf{d}$ and the Euler angle rotation Θ. The latter can be used to define a rotation matrix $\mathbb{R}$, which can be written, for instance, as in [9], in terms of Euler angles according to the *xyz*-convention in the rotation order, as:

$$\mathbb{R} = \begin{pmatrix} \mathrm{c}\psi\mathrm{c}\theta & -\mathrm{s}\psi\mathrm{c}\phi + \mathrm{c}\psi\mathrm{s}\theta\mathrm{s}\phi & \mathrm{s}\psi\mathrm{s}\phi + \mathrm{c}\psi\mathrm{s}\theta\mathrm{c}\phi \\ \mathrm{s}\psi\mathrm{c}\theta & \mathrm{c}\psi\mathrm{c}\phi + \mathrm{s}\psi\mathrm{s}\theta\mathrm{s}\phi & -\mathrm{c}\psi\mathrm{s}\phi + \mathrm{s}\psi\mathrm{s}\theta\mathrm{c}\phi \\ -\mathrm{s}\theta & \mathrm{c}\theta\mathrm{s}\phi & \mathrm{c}\theta\mathrm{c}\phi \end{pmatrix}, \tag{5}$$

where $\mathrm{s}\cdot = \sin(\cdot)$ and $\mathrm{c}\cdot = \cos(\cdot)$.

The translational velocity of the body with respect to the inertial reference frame can be related to the linear velocity in the non-inertial reference frame by the following equation:

$$\dot{\mathbf{d}} = \mathbb{R}\mathbf{v}, \tag{6}$$

vice versa,

$$\mathbf{v} = \mathbb{R}^{-1}\dot{\mathbf{d}} = \mathbb{R}^T\dot{\mathbf{d}}, \tag{7}$$

as $\mathbb{R}$ is an orthogonal matrix.

The angular velocity Ω in the non-inertial reference frame can be related to the time rate of change of the Euler angles as follows

$$\dot{\Theta} = \mathbb{Q}\Omega, \tag{8}$$

where $\mathbb{Q}$ is the transformation matrix given by

$$\mathbb{Q} = \begin{pmatrix} 1 & \mathrm{s}\phi\mathrm{s}\theta/\mathrm{c}\theta & \mathrm{c}\phi\mathrm{s}\theta/\mathrm{c}\theta \\ 0 & \mathrm{c}\phi & -\mathrm{s}\phi \\ 0 & \mathrm{s}\phi/\mathrm{c}\theta & \mathrm{c}\phi/\mathrm{c}\theta \end{pmatrix}. \tag{9}$$

And the inverse transformation is

$$\Omega = \mathbb{Q}^{-1}\dot{\Theta} = \begin{pmatrix} 1 & 0 & -\mathrm{s}\theta \\ 0 & \mathrm{c}\phi & \mathrm{c}\theta\mathrm{s}\phi \\ 0 & -\mathrm{s}\phi & \mathrm{c}\theta\mathrm{c}\phi \end{pmatrix}\dot{\Theta}. \tag{10}$$

It is clear Eq. (9) fails for $\theta = 90^\circ$. This usually is not an issue for many systems as they are not disigned to have such an operational condition. Nontheless, quaternions can be adopted to avoid this singularity.

Navier–Stokes Equations

In the inertial reference frame defined above, the Navier–Stokes equations governing the incompressible viscous flows can be written as:

$$\frac{\partial \mathbf{u}}{\partial t} + \nabla\cdot\mathbf{u}\mathbf{u} = \frac{1}{\mathrm{Re}}\nabla^2\mathbf{u} + \mathbf{f}, \tag{11}$$
$$\nabla\cdot\mathbf{u} = 0, \tag{12}$$

where t is the time, $\mathbf{f}$ represents the momentum forcing term due to the immersed body. The above equations have been non-dimensionalized using a reference length scale L and reference velocity scale U. Hence the Reynolds number in Eq. (11) is defined as $\mathrm{Re} = \rho_f UL/\mu$ with ρ_f the density of the fluid and μ the dynamic viscosity.

Equations for Rigid Body Dynamics

The dynamics of a rigid body in a fluid-structure coupled system is described by Newton's second law and Euler's equation in the body-fixed non-inertial reference frame:

$$\mathbb{M}_\mathrm{s}\frac{\mathrm{d}\mathbf{v}}{\mathrm{d}t} + \mathbb{M}_\mathrm{s}\Omega\times\mathbf{v} = \mathbf{F}_\mathrm{N} + \mathbf{E}_\mathrm{N}, \tag{13}$$
$$\mathbb{I}_\mathrm{s}\frac{\mathrm{d}\Omega}{\mathrm{d}t} + \Omega\times(\mathbb{I}_\mathrm{s}\Omega) = \mathbf{T}_\mathrm{N} + \mathbf{S}_\mathrm{N}, \tag{14}$$

where $\mathbb{M}_\mathrm{s}$ is the mass of the solid body, m_s, times a 3×3 identity matrix (tensor) $\mathbb{I}$, $\mathbb{I}_\mathrm{s}$ is the moment of inertia of the body, $\mathbf{F}_\mathrm{N}$ and $\mathbf{T}_\mathrm{N}$ are the fluid force and moment in the non-inertial reference frame, respectively. The force and moment $\mathbf{F}_\mathrm{N}$ and $\mathbf{T}_\mathrm{N}$ can be transformed to those in the inertial reference frame as

$$\mathbf{F}_\mathrm{I} = \mathbb{R}\mathbf{F}_\mathrm{N}, \tag{15}$$
$$\mathbf{T}_\mathrm{I} = \mathbb{R}\mathbf{T}_\mathrm{N}, \tag{16}$$

respectively. Likewise, all other sources of force and moment applied on the body in the non-inertial reference frame are represented by $\mathbf{E}_\mathrm{N}$ and $\mathbf{S}_\mathrm{N}$, respectively. The external force $\mathbf{E}_\mathrm{N}$ can

be obtained from that in the inertial reference frame using the following transformation:

$$\mathbf{E}_{\mathrm{N}} = \mathbb{R}^T \mathbf{E}_{\mathrm{I}}, \tag{17}$$

and the external force in inertial reference frame is given by

$$\mathbf{E}_{\mathrm{I}} = -\mathbb{C}\dot{\mathbf{d}} - \mathbb{K}\mathbf{d} + (\mathbb{M}_{\mathrm{s}} - \mathbb{M}_{\mathrm{f}})\mathbf{g}, \tag{18}$$

with $\mathbb{C}$ the damping matrix, $\mathbb{K}$ the stiffness matrix, $\mathbf{g}$ the gravitational acceleration, and $\mathbb{M}_{\mathrm{f}} = m_{\mathrm{f}}\mathbb{I} = \rho_{\mathrm{f}} V_{\mathrm{s}}\mathbb{I}$ the mass matrix of the fluid displaced by the solid body of volume V_{s}. Note that the external moment on the body, $\mathbf{E}_{\mathrm{N}}$, can be defined in a similar manner except that the anchor points of the springs may be fixed in the inertial reference frame or following the rigid body motion, and the angular velocity Ω can be related to the time rate of change of the Euler angles $\dot{\Theta}$ directly only in the one DOF (degree-of-freedom) rotation cases.

NUMERICAL METHOD

Navier–Stokes Solver

The details of many aspects of the numerical method used in this work have been presented in several previous studies [5, 6, 10]. A fractional-step method is employed for velocity-pressure coupling, in which a pressure Poisson equation is solved to enforce the continuity equation. A semi-implicit scheme is used for time advancement with the second-order Adams–Bashforth scheme for the convection terms and the Crank–Nicolson scheme for the viscous terms. The spatial derivatives are discretized using second-order central difference schemes on a staggered Cartesian grid, on some under-resolved grids higher-order upwind schemes are applied to the convective terms for better numerical stability. Approximate factorization method is used for the discretized momentum equations and a parallel tridiagonal solver is then applied to invert the linear systems. The Poisson equation is solved using either a direct solver from the FISHPACK library [11] or a semi-coarsening multigrid solver from the Hypre package [12].

Immersed Boundary Treatment

In a direct forcing immersed boundary method, a major task is the evaluation of the momentum forcing term to represent the effect of an immersed rigid body on the fluid flow. Depending on the specific approach used, this step can be quite different. Here, a simple and straightforward approach is adopted by directly reconstructing the solution near the immersed boundary such that the boundary conditions on the immersed boundary are satisfied. At the forcing points, which are points in the fluid phase but with neighboring point in the solid phase, a local reconstruction is

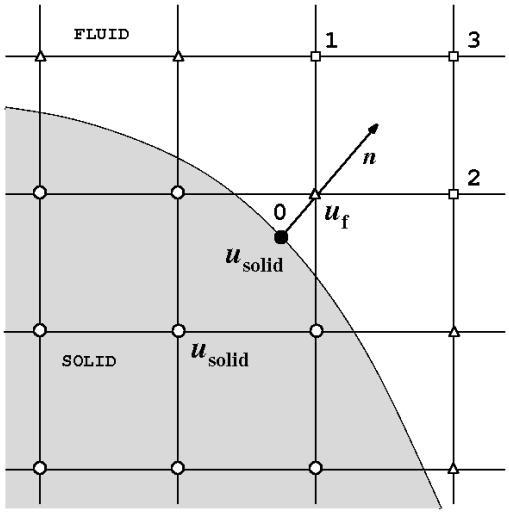

FIGURE 2. IMMERSED BOUNDARY TREATMENT.

necessary to obtain $\mathbf{u}_f^n$. We use a linear interpolation stencil, which include one point on the immersed boundary ($\mathbf{u}_{solid}^n$) and three (two for 2D cases) fluid points near the forcing point, as shown in Fig. 2, to reconstruct the expected $\mathbf{u}_f^n$ using the auxiliary velocity field $\tilde{\mathbf{u}}$. For details, the reader is referred to [5] and [6]. Note that $\mathbf{u}_{solid}^n$ is unknown in a fluid-structure interaction problem and has to be obtained by solving the dynamic equations for rigid body motion.

In [5], a field extension strategy was proposed to recover the physical values of pressure/velocity derivatives at the fluid points which were forcing points at the previous time step. This field extension can be implemented by extrapolating the physical information from the flow field into the regions containing non-physical information before the immersed boundary is relocated at each time step. For velocity components, the non-physical region can be easily defined as the grid points covered by the immersed body (for under-resolved grids or geometries with lower dimensions than the grids, the definition will involve those neighboring points of a forcing point that are in the fluid too). However, the extension for pressure field is performed on points that are selected based on their association with non-physical velocity points due to the staggering of the grid. The reader is referred to [5] for more details. The overall field extension strategy is quite successful by eliminating spurious forces generated near the immersed boundary, as shown in the results given in [5] for prescribed motion and [6] for predicted motion. Note that FSI applications are very sensitive to spurious force oscillation, especially when the light structures with density close to or less than the fluid density. The robustness of the strong coupling FSI algorithm in [6] also shows the effectiveness of the field extension strategy.

Here we propose a simple and effective version of the field

extension strategy for the pressure field. In [5], the boundary condition for pressure

$$\left(\frac{\partial p}{\partial n}\right)|_\Gamma = -\left(\frac{\mathrm{D}\mathbf{u}}{\mathrm{D}t}\cdot\mathbf{n}\right)|_\Gamma, \tag{19}$$

was used to extend physical pressure information into the regions with non-physical pressure values. Notice that the purpose of this pressure extension is to fix the non-physical pressure gradient components at those velocity forcing points, we can actually fix components of the pressure gradient at the velocity forcing points directly. At the immersed boundary, the boundary condition for components of the pressure gradient can be written as

$$\left(\frac{\partial p}{\partial x_i}\right)|_\Gamma = -\left(\frac{\mathrm{D}u_i}{\mathrm{D}t}\right)|_\Gamma, \tag{20}$$

where x_i ($i = 1,2,3$ for 3D and $i = 1,2$ for 2D problems) is the ith Cartesian coordinate and u_i is the corresponding Cartesian velocity component. This equation gives the Dirichlet boundary condition for the ith component of the pressure gradient, which is also collocated with the ith velocity component. Therefore, the reconstruction stencil for the velocity component can be directly used to interpolate the corresponding component of the pressure gradient at the same location. Comparing to the extrapolation of pressure itself in [5], this step represents a great simplification of the whole procedure for immersed boundary treatment. The pressure points requiring field extension are no longer necessary to be defined and all associated data structures and computational overhead are eliminated. The only extra expense is some temporary memory space to store the pressure gradient, which has to be evaluated in the original approach anyway.

ODE Solver for Rigid Body Dynamics

As in [6], Hamming's 4th-order predictor-corrector scheme is used to solve the governing equations for rigid body dynamics. First, the equations are rewritten as a system of non-dimensionalized, $2n$ first-order ordinary differential equations (n is the degrees of freedom of the structures). One equation from this system can be given as

$$\dot{q} = \frac{\mathrm{d}q}{\mathrm{d}t} = f(t,q), \tag{21}$$

where q represents the displacement or velocity in a certain direction. With Hamming's scheme [13], we have three steps:

1. predictor step: the solution is explicitly predicted and then modified using error estimate from the previous time step

$$q_p^n = q^{n-4} + \frac{4}{3}\Delta t\left(2\dot{q}^{n-1} - \dot{q}^{n-2} + 2\dot{q}^{n-3}\right), \tag{22}$$

$$q_c^{k=0} = q_p^n - \frac{112}{121}\left(q_p^{n-1} - q_c^{n-1}\right), \tag{23}$$

   where subscripts p and c represent the predicted and corrected values, respectively, and superscript k is the iteration index for the corrector step.
2. corrector step: the solution from above is corrected iteratively

$$\begin{aligned} &\text{for} \quad k = 1,\cdots,m \\ &\quad q_c^k = \frac{1}{8}\left(9q^{n-1} - q^{n-3}\right) + \frac{3}{8}\Delta t\left(2\dot{q}_c^{k-1} + 2\dot{q}^{n-1} - \dot{q}^{n-2}\right) \\ &\quad \text{if} \quad |q_c^k - q_c^{k-1}| < \varepsilon, \quad q_c^n = q_c^k, \quad \text{exit.} \end{aligned} \tag{24}$$

   where m is the maximum number of iterations and ε is the tolerance ($\varepsilon = 10^{-8}$ is used in the present study). And this convergence criterion has to be met for all equations in the system before the iteration can be terminated.
3. finalizer step: the solution is updated using the estimated truncation error

$$q^n = q_c^n + \frac{9}{121}\left(q_p^n - q_c^n\right). \tag{25}$$

This scheme is very robust and efficient as shown in [6].

RESULTS

In this part, a case with prescribed motion is presented first to establish the accuracy of the reformulated field extension and force calculation. Then a circular cylinder freely oscillating in a free stream is used to validate our FSI algorithm and demonstrate the efficiency. The last case is a rectangular plate in a free fall fluttering in a fluid.

In-Line Oscillation of a Circular Cylinder

In this case, a circular cylinder is forced to do a prescribed translational motion in a fluid at rest. The equation of motion is given by $x(t) = -A\sin(2\pi ft)$, where A is the oscillation amplitude. Two key parameters are the Reynolds number, $Re = U_{\max}D/\nu$, and the Keulegan-Carpenter number, $KC = U_{\max}/fD$, where $U_{\max}$ is the maximum velocity of the cylinder, D is the diameter of the cylinder, ν is the kinematic viscosity of the fluid, and f is the characteristic frequency of the oscillation. The parameters from the experiments and numerical simulations in [14]

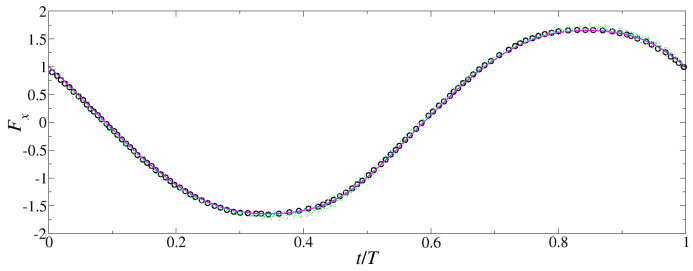

FIGURE 3. TIME HISTORY OF THE IN-LINE FORCE ACTING ON A CYLINDER OSCILLATING IN A FLUID AT REST AT $RE = 100$ AND $KC = 5$. $\circ$: EXPERIMENTAL DATA [14]; ····· : GRID 120×240; – – – : GRID 240×480; —— : GRID 480×960.

were used here, i.e., $Re = 100$ and $KC = 5$. The size of computational domain is $40D \times 24D$ in the x and y directions, respectively, with the cylinder located at the center initially. Three different grids of 240×120, 480×240, and 960×480 were used for this case and around the cylinder the grids were approximately uniform in both directions with spacings of $0.01D$, $0.02D$, and $0.04D$, respectively. A constant time step of $0.005D/U_{\max}$ was used on all three grids.

The computations were performed until periodic vortex shedding was established for all cases. Figure 3 shows the time history of the in-line force, $F_x(t)$, acting on the cylinder. Results from all three grids are in very good agreement with the reference data from [14]. This validates our simplified approach for applying the pressure field extension is accurate.

Figure 4 shows the pressure and vorticity contours at four different phase-angles from the fine grid simulation. The results are in very good agreement with the corresponding results reported in [14].

Free X-Y Oscillation of A Circular Cylinder

The fluid-structure interaction problem of an elastically mounted circular cylinder in a free stream was considered to show the accuracy of our new formulation. The cylinder can be modeled as a mass-spring-damper system, and the governing equations for the cylinder motion are as follows:

$$\ddot{x} + 2\zeta\left(\frac{2\pi}{U^*}\right)\dot{x} + \left(\frac{2\pi}{U^*}\right)^2 x = \frac{2}{\pi m^*}C_D, \tag{26}$$

$$\ddot{y} + 2\zeta\left(\frac{2\pi}{U^*}\right)\dot{y} + \left(\frac{2\pi}{U^*}\right)^2 y = \frac{2}{\pi m^*}C_L, \tag{27}$$

where the mass ratio is $m^* = m_s/m_f$, the reduced velocity is $U^* = U_\infty/f_N D$. The natural vibration frequency of the structure and the

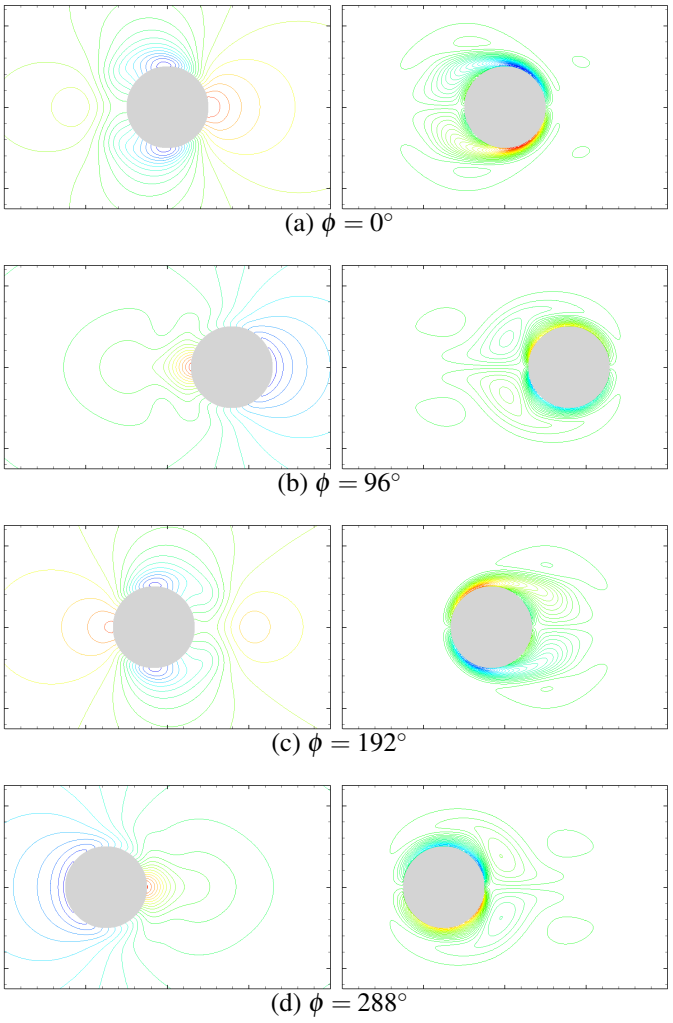

FIGURE 4. PRESSURE (LEFT) AND VORTICITY (RIGHT) CONTOURS AT FOUR DIFFERENT PHASE-ANGLES FOR AN IN-LINE OSCILLATING CYLINDER IN A FLUID AT REST AT $RE = 100$ AND $KC = 5$.

damping ratio are given by

$$f_N = \frac{1}{2\pi}\sqrt{k/m_s}, \quad \zeta = \frac{1}{2}c\sqrt{km_s}, \tag{28}$$

respectively, where k is the spring constant and c is the damping coefficient. the drag and lift coefficients are defined as

$$C_D = \frac{f_x}{\frac{1}{2}\rho_f D L_c U_\infty^2}, \quad C_L = \frac{f_y}{\frac{1}{2}\rho_f D L_c U_\infty^2}, \tag{29}$$

with L_c is the span of the cylinder, f_x and f_y the instantaneous drag and lift forces on the cylinder, respectively. Also, $x = X_o/D$

and $y = Y_o/D$ are the non-dimensionalized horizontal and vertical displacements with X_o and Y_o the streamwise and transverse displacement of the cylinder center. Note that the same length and velocity reference scales as in the Navier-Stokes equations (the cylinder diameter, D, and the freestream velocity, U_∞) were used here.

The parameters were selected to match the spectral element simulation in a non-inertial reference frame in [15]. The Reynolds number is $\mathrm{Re} = 200$, the reduced velocity is $U* = 5.0$, the damping ratio is $\zeta = 0.01$, and the mass ratio is $m* = 4/\pi$. In our simulation, the inflow of a uniform velocity U_∞ is located $10D$ upstream of the cylinder. The outflow boundary is located $30D$ downstream of the cylinder and a convective boundary condition is applied. Both top and bottom boundaries are located $10D$ away from the cylinder and a freestream condition is used. Three different grids were used to cover the whole domain and the number of grid points for the three grids are 160×120, 320×240, and 640×480 in the streamwise and transverse directions, respectively. The grids were stretched in both directions. Near the cylinder, the grid spacings were $0.04D \times 0.04$, $0.02D \times 0.02D$, and $0.01D \times 0.01D$, respectively. A constant time step of $0.004D/U_\infty$ was used for all three grids.

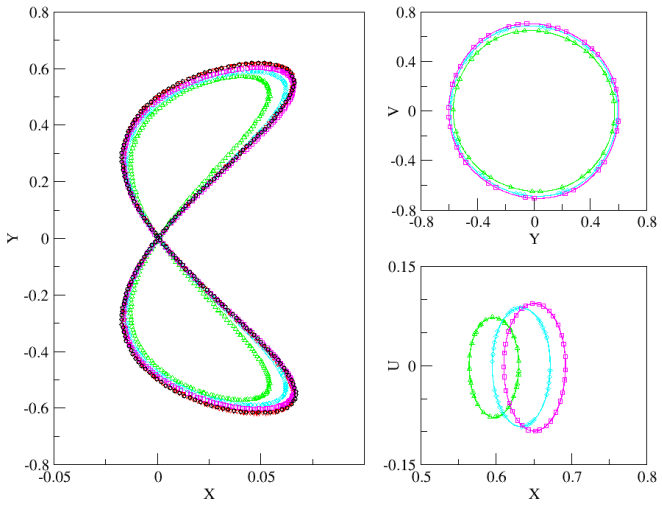

FIGURE 5. CENTERLINE $X-Y$ DISPLACEMENT AND DISPLACEMENT-VELOCITY PHASE PLOTS FOR A CIRCULAR CYLINDER FREELY VIBRATING IN THE (X,Y) PLANE. $\circ$: SPECTRAL ELEMENT SIMULATION IN A NON-INERTIAL REFERENCE FRAME [15]; $\triangledown$: PREVIOUS IMMERSED BOUNDARY SIMULATION [6]; $\triangle$: GRID 120×160; $\diamond$: GRID 240×320; $\square$: GRID 480×640.

On all three grids, the simulations were carried out first with fixed cylinders. After the periodic vortex shedding pattern was established, the cylinder was released to have two degrees of freedom in both streamwise and transverse directions. All simulations had been run until a stable periodic state was reached and enough shedding cycles were obtained. Figure 5 shows the centerline displacement and displacement-velocity phase plots. The centerline displacement data from [15] using a high order spectral element method in a non-inertial reference frame and from a previous immersed boundary simulation [6] are also given in the figure. All the centerline displacement data have been shifted to have the "figure of eight" plots from all cases centered at $(0,0)$. Our fine grid results match the reference data very well and there is a clear trend of grid convergence of the solution, which can be seen from the displacement-velocity phase plots as well.

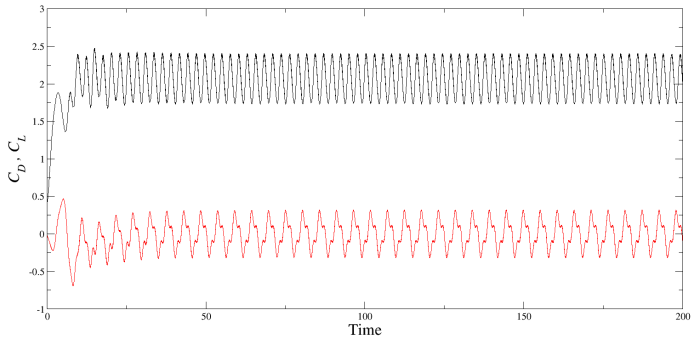

FIGURE 6. TIME SERIES OF LIFT AND DRAG COEFFICIENTS FOR A CIRCULAR CYLINDER FREELY VIBRATING IN THE (X,Y) PLANE.

Figure 6 shows the time series of the lift and drag coefficients from the fine grid simulation. It is evident that a short period of transient oscillation was experienced after the cylinder was released from stationary state and very soon the stable periodic state was achieved. Fig. 7 shows the instantaneous vorticity contours from the free oscillating cylinder, which gives a clear 2S vortex pattern that has been observed in many experiments and simulations.

It is worth noting that the same convergence criterion $\varepsilon = 10^{-8}$ as [6] was used in simulations on all three grids. On the fine grid about 4 iterations in average were used in each time step. Since there is a predictor step and finalizer step, a total of 6 times of displacing the immersed body. With the previous algorithm, the averaged number of iterations was about the same, but the cost is at least 5 times higher as the full system of fluid solver was included in each iteration. For complex cases that require more iterations, our current algorithm may result in an acceleration of

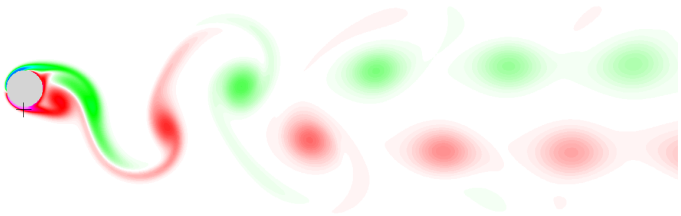

FIGURE 7. INSTANTANEOUS VORTICITY CONTOURS FOR FOR A CIRCULAR CYLINDER FREELY VIBRATING IN THE (X,Y) PLANE, THE $+$ MARKS THE ORIGINAL LOCATION THE CYLINDER WAS RELEASED.

one order of magnitude in term of the computational speed for completing the whole simulation.

A Fluttering Rectangular Plate

In this case, a rectangular plate of size $L \times H$, where H is the thickness and $L = 14H$ the width of the plate, was released in a fluid at rest. The density of the plate is $\rho_s = 2.71\rho_f$. The gravitational acceleration is g. Depending on the thickness/width ratio and the initial condition, the plate may do complicated fluttering, tumbling, or chaotic combined fluttering/tumbling motions. A terminal velocity for the plate can be defined as

$$U_t = \sqrt{2Hg\left(\frac{\rho_s}{\rho_f} - 1\right)}. \tag{30}$$

The Reynolds number can be defined using this terminal velocity as $Re = U_t L/\nu$ with ν the kinematic viscosity of the fluid. In this case, the Reynolds number was 210. The computational domain was $5.3L \times 14L$ in the horizontal and vertical directions, respectively. A uniform grid of 300×800 was used with a resolution of about $0.25H \times 0.25H$. The initial angle of the plate was 45 degrees and the plate was placed near the top of the domain when it was released at $t = 0$.

Figure 8 shows the instantaneous vorticity contours at several instants during the fall of the plate. For the current setup, the plate developed periodic fluttering motion very soon after it was released, which is also shown in Fig. 9 for time series of linear and angular velocities of the plate. The results here qualitatively agree well with reference experimental and computational results available in the literature. But further validation is needed for detailed quantitative comparison.

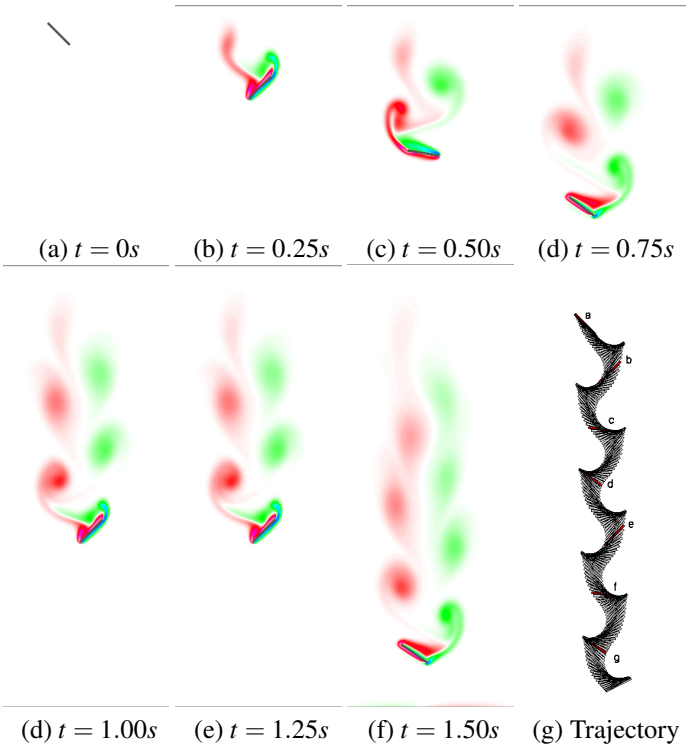

(a) $t = 0s$ (b) $t = 0.25s$ (c) $t = 0.50s$ (d) $t = 0.75s$

(d) $t = 1.00s$ (e) $t = 1.25s$ (f) $t = 1.50s$ (g) Trajectory

FIGURE 8. INSTANTANEOUS VORTICITY CONTOURS AT SEVERAL INTANTS FOR A FREE FALLING PLATE FLUTTERING IN A FLUID. THE LAST FIGURE (G) SHOWS THE OVERLAID TRAJECTORY OF THE PLATE.

CONCLUSIONS AND FUTURE WORK

In this work, we have successfully simplified the sharp interface immersed-boundary method in [5] by using a reformulated pressure field extension approach and expedited the strong coupling algorithm in [6] for FSI problems by taking the fluid solver out of the FSI iterations. The resulting FSI strong coupling method is very efficient without losing any accuracy from the previous formulation. An acceleration of several times or even one order of magnitude can be achieved with our current approach.

Future work includes extending the current method for two-phase flows interacting with moving bodies and adding an immersed boundary based wall model to the local reconstruction for high Reynolds number flows. In [16], we extended the sharp interface immersed-boundary/level-set method in [10] to strongly coupled wave-body interactions by using a non-inertial reference frame. One limitation with this approach is that when large-angle rotation is involved, the original Cartesian grid designed for resolving the air-water interface and the structure may not have a good resolution for air-water interface away from the structure. And the implementation of wall-modeled local reconstruction on top of the approach in [16] could be cumbersome. Our current approach can avoid these two issues by using a limited extent of iterative operations. The wall function approach developed in [17, 18] needs very fine resolution near the wall boundaries.

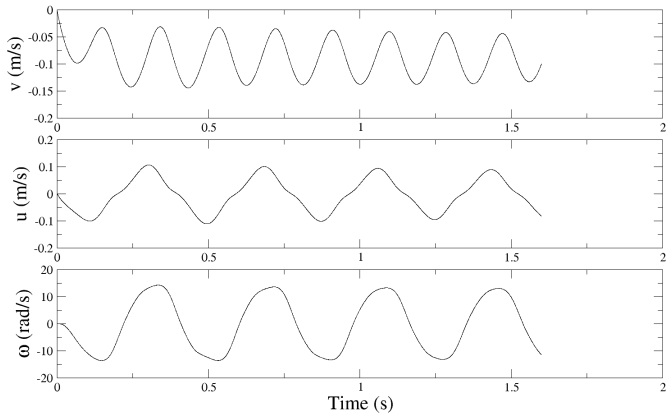

FIGURE 9. TIME HISTORY OF THE LINEAR AND ANGULAR VELOCITIES OF A FREE FALLING PLATE FLUTTERING IN A FLUID.

In [19] some prelimilary work to improve it by decoupling the pressure and the velocity jump at the immersed boundary was reported using an approximate domain approach. Nonetheless, further studies are required for developing a wall-modeled immersed boundary method that can be used for simulating wave-body interactions in ship hydrodynamics.

ACKNOWLEDGMENT

This work was sponsored by the Office of Naval Research (ONR) under grant N000141-01-00-1-7, with Dr. Patrick Purtell as the program manager.

REFERENCES

[1] Fadlun, E. A., Verzicco, R., Orlandi, P., and Mohd-Yusof, J., 2000. "Combined immersed-boundary finite-difference methods for three-dimensional complex flow simulations". *Journal of Computational Physics,* ***161***(1), pp. 35 – 60.

[2] Kim, J., Kim, D., and Choi, H., 2001. "An immersed-boundary finite-volume method for simulations of flow in complex geometries". *Journal of Computational Physics,* ***171***(1), pp. 132 – 150.

[3] Tseng, Y.-H., and Ferziger, J. H., 2003. "A ghost-cell immersed boundary method for flow in complex geometry". *Journal of Computational Physics,* ***192***(2), pp. 593 – 623.

[4] Balaras, E., 2004. "Modeling complex boundaries using an external force field on fixed cartesian grids in large-eddy simulations". *Computers & Fluids,* ***33***(3), pp. 375 – 404.

[5] Yang, J., and Balaras, E., 2006. "An embedded-boundary formulation for large-eddy simulation of turbulent flows interacting with moving boundaries". *Journal of Computational Physics,* ***215***(1), pp. 12–40.

[6] Yang, J., Preidikman, S., and Balaras, E., 2008. "A strongly coupled, embedded-boundary method for fluid-structure interactions of elastically mounted rigid bodies". *Journal of Fluids and Structures,* ***24***(2), pp. 167–182.

[7] Vanella, M., Fitzgerald, T., Preidikman, S., Balaras, E., and Balachandran, B., 2009. "Influence of flexibility on the aerodynamic performance of a hovering wing". *J Exp Biol,* ***212***(1), pp. 95–105.

[8] Kim, D., and Choi, H., 2006. "Immersed boundary method for flow around an arbitrarily moving body". *Journal of Computational Physics,* ***212***(2), pp. 662–680.

[9] Fossen, T. I., 1994. *Guidance and Control of Ocean Vehicles*. John Wiley & Sons, New York, NY.

[10] Yang, J., and Stern, F., 2009. "Sharp interface immersed-boundary/level-set method for wave-body interactions". *Journal of Computational Physics,* ***228***(17), pp. 6590–6616.

[11] Swarztrauber, P. N., 1974. "A direct method for the discrete solution of separable elliptic equations". *SIAM Journal on Numerical Analysis,* ***11***(6), pp. pp. 1136–1150.

[12] Falgout, R., Jones, J., and Yang, U., 2006. "The design and implementation of hypre, a library of parallel high performance preconditioners". In *Numerical Solution of Partial Differential Equations on Parallel Computers*, A. Bruaset and A. Tveito, eds., Vol. 51. Springer-Verlag, pp. 267–294. UCRL-JRNL-205459.

[13] Hamming, R. W., 1959. "Stable predictor-corrector methods for ordinary differential equations". *J. ACM,* ***6***, January, pp. 37–47.

[14] Dütsch, H., Durst, F., Becker, S., and Lienhart, H., 1998. "Low-Reynolds-number flow around an oscillating circular cylinder at low Keulegan–Carpenter numbers". *Journal of Fluid Mechanics,* ***360***, pp. 249–271.

[15] Blackburn, H. M., and Karniadakis, G. E., 1993. "Two and three dimensional simulations of vortex-induced vibration of a circular cylinder". In Third International Offshore and Polar Engineering Conference, pp. 715–720.

[16] Yang, J., and Stern, F., 2010. "Efficient simulation of fully coupled wave-body interactions using a sharp interface immersed-boundary/level-set method". In Proceedings of ASME 2010 3rd Joint US-European Fluids Engineering Summer Meeting and 8th International Conference on Nanochannels, Microchannels, and Minichannels, no. FEDSM-ICNMM2010-30103. Montreal, Canada.

[17] Yang, J., Bhushan, S., Suh, J., Wang, Z., Koo, B., Sakamoto, N., Xing, T., and Stern, F., 2008. "Large-eddy simulation of ship flows with wall-layer models on Cartesian grids". In Proceedings of the 27th Symposium on Naval Hydrodynamics. Seoul, Korea.

[18] Bhushan, S., Carrica, P. M., Yang, J., and Stern, F., 2011.

"Scalability studies and large grid computations for surface combatant using CFDShip-Iowa". *International Journal of High Performance Computing Applications*. in press.

[19] Yang, J., Michael, T., Bhushan, S., Akira, H., Wang, Z., and Stern, F., 2008. "Motion prediction using wall-resolved and wall-modeled approaches on a Cartesian grid". In Proceedings of the 28th Symposium on Naval Hydrodynamics. Pasadena, CA.